Surface Skin Temperature and Its Trend Observations From IASI on Board MetOp Satellites

Daniel K. Zhou, Allen M. Larar, and Xu Liu

***Abstract*—Global surface skin temperature has been retrieved from MetOp IASI ultraspectral infrared measurements over the past 13+ years. Monthly and spatially gridded surface skin temperature is produced to show some phenomena associated with its natural variability. This article has aimed to demonstrate that thermal infrared remote sensing data can be used for monitoring global surface environmental characteristics and associated change through the continuity observations of MetOp series. The time-series anomalies of surface skin temperature are used to estimate its associated trend. Error estimation and evaluation has been performed and discussed in order to understand the uncertainty and variability in the trends. The trends derived from IASI global surface skin temperatures are compared with those of the NASA GISS global surface air temperature. Despite the physical differences between surface skin and air temperatures, reasonable agreement is shown between these two datasets indicating consistency and global surface warming, achieving our core objective of investigating the surface skin temperature retrieved from MetOp satellites' measurements and associated trends. The inferred trend of IASI global surface skin temperature illustrates an approximate 0.037±0.002 K/yr. global average increase has occurred during the September 2007—present (November 2020) time period; this warming trend is more pronounced in the northern hemisphere.**

***Index Terms*—Global warming, infrared measurements, remote sensing, satellite, temperature.**

I. Introduction

GLOBAL or regional surface air temperature analyses are routinely performed to monitor global climate change by many groups such as the NOAA National Centers for Environmental Information, the Hadley Centre of the U.K. Met Office and the University of East Anglia Climate Research Unit, and the NASA Goddard Institute for Space Studies (GISS). Very similar data sources of surface temperatures are often used in studies for environment and climate change detection and/or monitoring by different groups [1]–[3]; however, there are different ways to use or interpolate the data to regional or global scales. Surface temperature trend analysis results partly depend on the ways data were handled [4] and do actually represent "near surface" air temperatures ($T_{\rm sa}$). A warming trend of global surface air, at a rate of approximately 0.15–0.20 K per decade, has been previously reported for recent decades (∼1970–2010) [2], [5]. Existing effective surface temperature products show a large degree of variance because they are highly dependent upon the specific determination and interpolation methodology utilized. This exemplifies the need for more representative estimates to contribute toward better characterization of these surface parameter geophysical fields and their associated uncertainties.

Techniques utilizing satellite remote sensing data from polar orbiting platforms offer a unique contribution since they could provide global coverage with relatively rapid temporal refreshing and denser spatial sampling. Global surface parameters like surface skin temperature ($T_{\rm ss}$) and emissivity (ε_ν) are important parameters in physical processes of the Earth's surface, such as energy fluxes between the surface and atmosphere, and water balance on regional or global scales [2], [6]. These surface parameters also provide information on the surface equilibrium state of temporal and spatial variability [6]. $T_{\rm ss}$ is derived from upwelling longwave radiation from the Earth's surface based on Planck's radiation law (or Stefan-Boltzmann law), and it can be retrieved from aircraft and/or satellite infrared-thermal-radiometric measurements. $T_{\rm sa}$ is an air kinetic temperature measured by an *in situ* thermometer near the Earth's surface. A more detailed definition of the Earth's surface skin temperature and how it differs from surface air temperature (i.e., air temperature at 1.5–2 m above the Earth's surface) can be found elsewhere [7]. High-altitude aircraft- and satellite-based measurements of thermal infrared (TIR) spectral radiances are uniquely capable of observing temperatures across the planetary boundary layer as they are directly associated with surface and atmospheric (including cloud) parameters. For example, a planetary boundary layer temperature inversion was measured in TIR radiances during the Second Suomi-NPP Calibration/Validation Campaign over the Greenland ice-sheet—where the surface skin was extremely colder than surface air [8]. $T_{\rm ss}$ retrieved from remotely sensed spectral radiance is based on Planck's law or the radiative transfer equation; surface emissivity knowledge is crucial for achieving other highly accurate retrieved parameters such as surface skin temperature [6].

Advanced satellite ultraspectral infrared sounders have been developed and flown in space for more than a decade since the launch of the Atmospheric Infrared Sounder (AIRS) on the Aqua satellite (2002) [9], the Interferometer Atmospheric Sounding Instrument (IASI) on the MetOp-A (2006), MetOp-B (2012), and MetOp-C (2018) [10], [11], and the Cross-track Infrared Sounder (CrIS) on the Suomi-NPP (2011) and the

Manuscript received October 6, 2020; revised December 16, 2020; accepted December 16, 2020. Date of publication December 21, 2020; date of current version January 13, 2021. This work was supported in part by the NOAA JPSS Program Science Office, NASA Headquarters, and NASA Langley Research Center performed under the NAST-I program. *(Corresponding author: Daniel K. Zhou.)*

The authors are with NASA Langley Research Center, Hampton, VA 23681 USA (e-mail: daniel.k.zhou@nasa.gov; allen.m.larar@nasa.gov; xu.liu-1@nasa.gov).

Digital Object Identifier 10.1109/JSTARS.2020.3046421

JPSS-1 (2017) satellites [12]. Retrieval algorithms have been developed by many groups for different space-based remote sensors [13]–[19] to enable retrieving $T_{\rm ss}$ and ε_ν from TIR ultraspectral measurements along with atmospheric profiles.

Satellite-measurement-derived Earth's surface skin temperature and its anomaly trends is useful to monitor our global environment, even though many studies and trend analyses have been done with Earth's $T_{\rm sa}$. $T_{\rm ss}$ and $T_{\rm sa}$ are physically different parameters and $T_{\rm ss}$ is relatively unrepresented in previous work. Our investigations on $T_{\rm ss}$ from regional to global distributions and their trends are presented in this communication to sustain or confirm NASA GISS analyses of global warming implied by $T_{\rm sa}$. One of the advantages of using satellite data from instruments onboard polar-orbiting platforms is having a global coverage, especially for remotely accessible regions where ground *in situ* observations are often absent. IASI measurements are used to obtain $T_{\rm ss}$ globally for analysis and assessment of trends from regional to global scales. Such global $T_{\rm ss}$ estimation can only be enabled by utilization of satellite remote sensing datasets. The objectives of this article are to retrieve and analyze $T_{\rm ss}$ from satellite TIR remote sensing measurements, to investigate the trend of time-series-retrievals obtained from associated satellite measurements, and to intercompare the trends with an independent analysis of $T_{\rm sa}$ to evaluate consistency of results and draw a conclusion. Preliminary outcomes from MetOp-A IASI measurements alone were briefly presented at the SPIE conference [20]. Now, up-to-date retrievals from all three MetOp satellites are used for analyzing and deriving $T_{\rm ss}$ trends; it is critical to bring all three MetOp satellites to this study as long-term continuity trending is essentially desired. Our results with detailed discussions are presented in this communication. Brief descriptions on IASI measurements and $T_{\rm ss}$ retrieval methodology, uncertainty evaluation, and continuity assessment between three MetOp satellites are given in Section II. Monthly 0.5°-latitude-longitude gridded datasets showing seasonal-cycles and interannual variations are presented in Section III. IASI regional and global $T_{\rm ss}$ trend results and discussions are given in Section IV, followed by conclusions in Section V.

II. Retrieval and Cross Satellite Evaluation

IASI was successfully launched into polar orbit aboard the operational MetOp-A satellite on October 19, 2006, MetOp-B satellite on September 19, 2012, and MetOp-C satellite on November 7, 2018. Three polar orbiting meteorological satellites (MetOp series) are all in the same sun-synchronous morning orbit. They are equally spaced around their orbits about 120° apart having a same Equator crossing time of 9:30 A.M. local solar time and a same inclination angle of 98.7° relative to the Equator. At a mean altitude of 817 km, they take about 100 min to complete one orbit. Having more than one satellite in the same orbit providing the same observation adds confidence in these measurements. Overlapping measurements allow us to cross-check on data consistency and extend the period for trend analysis. IASI is a Michelson interferometer. At nadir, the instrument samples data at intervals of 25 km along a cross track. Each sample has a maximum instantaneous field-of-view (IFOV) diameter of ∼12 km with continuous spectral coverage of 645 to 2760 $\rm cm^{-1}$ and an apodized spectral resolution of 0.5 $\rm cm^{-1}$ but sampled at 0.25 $\rm cm^{-1}$ [11], [21]. Significant scientific accomplishments have already been made with IASI measurements [11], for example, positive impact on NWP.

IASI higher spectral resolving power and its continuous spectral coverage benefit retrieving $T_{\rm ss}$ simultaneously with ε_ν and other atmospheric parameters. We have developed an inversion scheme, able to deal with cloudy as well as cloud-free radiances observed with ultraspectral TIR sounders, and applied it to IASI data for retrieving atmospheric thermodynamic and surface or cloud microphysical parameters simultaneously [16]. This retrieval algorithm was based on the algorithm originally developed for the National Airborne Sounder Testbed-Interferometer (NAST-I) [19]. NAST-I onboard NASA high-altitude research aircraft functions as a spaceborne instrument emulator. This retrieval algorithm has been evaluated through numerous airborne field calibration/validation campaigns [16], [19], [22]–[24]. NAST-I has a spectral coverage and spectral resolution nearly identical to the IASI instrument which not only simplifies algorithm evolution, but also subsequent validation. Accurate ε_ν retrieval is essential for correctly retrieving $T_{\rm ss}$ from a TIR spectrum, especially over land where it could be far less than a perfect blackbody (i.e., $\varepsilon_\nu < 1.0$) [6]. The continuous spectral coverage at high spectral resolution measurements of IASI provides the exact information needed to retrieve both $T_{\rm ss}$ and ε_ν simultaneously.

Following the terminology used by Strow *et al*. [25], retrieved ε_ν can be evaluated using its retrieval simulated radiance components. The surface is assumed to be Lambertian, and reflectivity is a function of surface emissivity such as

$$\rho_\nu^{\rm t} = (1-\varepsilon_\nu) \tag{1}$$

$$\rho_\nu^{\rm s} = (1-\varepsilon_\nu)/\pi \tag{2}$$

where $\rho_\nu^{\rm t}$ is the reflectance of the downwelling thermal flux $\rm F_\nu^d$ by the surface, and $\rho_\nu^{\rm s}$ is the solar reflectance of the surface. The channel radiance emitting from the top of a nonscattering, clear-sky atmosphere can be computed via a radiative transfer equation in terms of upwelling atmospheric emission (Atm-up, $\rm A_\nu^\uparrow$), downwelling atmospheric emission (Atm-down, $\rm A_\nu^\downarrow$), solar emission (Solar, S_ν), and surface emission (Ground, G_ν). Now, these components can be expressed as

$$\mathrm{A}_\nu^\uparrow = \int_{\mathrm{p_s}}^{0} \mathrm{B}_\nu\left[\mathrm{T}\left(\mathrm{p}\right)\right] \frac{\mathrm{d}\tau_\nu\left(\mathrm{p}\to 0, \theta_{\rm sat}\right)}{\mathrm{dp}}\mathrm{dp} \tag{3}$$

$$\mathrm{A}_\nu^\downarrow = \mathrm{F}_\nu^{\mathrm{d}}\tau_\nu\left(\mathrm{p_s}\to 0, \theta_{\rm sat}\right) \tag{4}$$

$$\mathrm{S}_\nu = \frac{\mathrm{H}_\nu}{\sec\left(\theta_{\rm sun}\right)\pi}\tau_\nu\left(0\to \mathrm{p_s}, \theta_{\rm sun}\right)\tau_\nu\left(\mathrm{p_s}\to 0, \theta_{\rm sat}\right) \tag{5}$$

$$\mathrm{G}_\nu = \mathrm{B}_\nu\left(\mathrm{T_{ss}}\right)\ \tau_\nu\left(\mathrm{p_s}\to 0, \theta_{\rm sat}\right) \tag{6}$$

where τ_ν is atmospheric transmittance, B_ν is the Planck function, p_s is surface pressure, *T(p)* is atmospheric temperature at pressure p, H_ν is the solar irradiance incident at the top of the atmosphere, $\theta_{\rm sat}$ and $\theta_{\rm sun}$ are satellite and sun zenith angles, respectively. Window channel emissivity can be derived

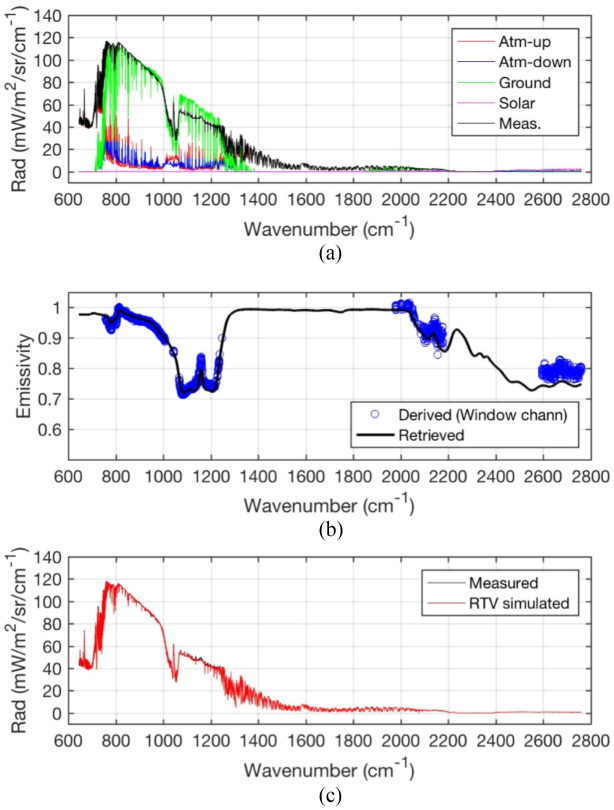

Fig. 1. Retrieved emissivity evaluation from IASI measurement of 09:23:10 UTC, January 16, 2013; 29.65°N latitude, 6.32°E longitude: (a) retrieval simulated radiance components and measured radiance, (b) derived emissivity compared with retrieved emissivity, and (c) measured and retrieval simulated radiance.

from measured radiance (R_ν) and retrieval simulated radiance components presented

$$\varepsilon_\nu = \frac{\mathrm{R}_\nu - \mathrm{A}_\nu^{\uparrow} - \mathrm{A}^{\downarrow}{}_\nu - \mathrm{S}_\nu}{\mathrm{G}_\nu - \mathrm{A}_\nu^{\downarrow} - \mathrm{S}_\nu}. \tag{7}$$

Fig. 1 shows an example of emissivity evaluation from Grand Erg Oriental, Algeria. Measured radiance and retrieval simulated radiance components described in (3)–(6) are plotted in Fig. 1(a). As shown in Fig. 1(b), window channel emissivity calculated from (7) is intercompared with retrieved emissivity. In conjunction with retrieved surface emissivity spectrum, T_{ss} of 291.51 K is accurately retrieved. As shown in Fig. 1(c), the measured and retrieval simulated radiances fit.

Validating these retrieved parameters (i.e., T_{ss} and ε_ν) over the global is the biggest challenge [6], [26]–[28], even though a few cases have already been evaluated for T_{ss}

1) From the Joint Airborne IASI Validation Experiment (JAIVEx) [16], [28], retrieved sea surface temperature was within an expected accuracy of 0.5 K and compared favorably with observations by all instruments from a variety of different platforms [16].
2) From the European Aqua Thermodynamic Experiment [22], T_{ss} over water was retrieved within an expected accuracy of 0.5 K by comparing ECMWF analysis and the retrievals from satellite and aircraft measurements [23].
3) From one of the early NAST-I field campaigns, the Chesapeake Lighthouse and Aircraft Measurements for Satellites, NAST-I retrieved T_{ss} is comparable to buoy measured bulk surface temperatures at the NOAA Chesapeake light buoy site [24].

The above evaluations were performed under clear-sky conditions with IASI or NAST-I single-footprint measurements over water. Detailed discussions on retrieval error estimation have also been given by using an error consistency analysis scheme [29]. From limited regional IASI measurements used for the analysis during JAIVEx, a total T_{ss} retrieval error, in terms of its bias and standard deviation error (bias, STDE) for land and water was estimated to be (−0.270 K, 0.349 K) and (−0.134 K, 0.362 K), respectively. From a simulation analysis over a global database, total T_{ss} retrieval error (bias, STDE) was estimated to be (0.25 K, 1.42 K) and (0.05 K, 0.97 K) over land and water, respectively [16].

Ground stations gather *in situ* T_{sa} measurements, but they are both fundamentally and physically different from satellite remotely sensed T_{ss} despite their spatial measure differences between a point and IFOV-mean. Their actual difference can be as large as 2 K or more under the conditions of locational homogeneity and weather [30]. Therefore, it is not practical to use *in situ* T_{sa} for remotely sensed T_{ss} validation based on T_{ss} retrieval accuracy that has been already achieved according to our knowledge. The intercomparison with other datasets like NWP models would also give relatively large differences (up to several degrees) due to their comparability and the nature of different data types. We believe that retrieval error estimated by an error consistency analysis scheme [29] is one of the best or more reliable ways for satellite retrieval evaluation.

There is a tremendous amount of data obtained from MetOp IASI measurements. In order to utilize and speed up data processing in the retrieval, we currently use an optimal physical regression retrieval scheme which identifies cloud and/or cloud-free conditions and retrieves surface T_{ss} and ε_ν [16], [27]. As surface emissivity retrieval improves, T_{ss} retrieval error is also reduced from the 2009 version to the 2011 version [17]. The STDE of T_{ss} is slightly larger from a physical regression than that from an optimal estimation retrieval. Conservatively, it should be less than 1.4 K but will depend on the atmospheric and surface condition of a single-footprint measurement. Since T_{ss} is not used under cloudy-sky conditions, there are some missing data from single-footprint retrievals. Here, we have assembled monthly 0.5°-latitude-longitude gridded datasets to ensure a full global coverage of the measurements. Now T_{ss} STDE of an assembled dataset is reduced, depending on how many data points are used in the grid point. Typically, from one satellite, the average data points in one month of 0.5°-latitude-longitude grid point is about 35–55 (excluding cloudy conditions), so, STDE of monthly gridded T_{ss} is reduced from that of single-footprint T_{ss} to about 0.2 K depending on the data point in a specific monthly grid point.

The data presented in this article are produced by a single FOV all-weather retrieval algorithm described elsewhere [16], [17] using MetOp IASI measurements from September 2007 to November 2020 (hereafter, refers to the analysis period)

TABLE I
GLOBAL T_{ss} MEAN BIAS, STDE, AND R^2 BETWEEN METOP SATELLITES DURING OVERLAPPING PERIOD

Satellite	Period (year.month)	Bias (K), STDE (K), R^2		
		Ascending Node	Descending Node	Combined Nodes
MetOp-A	2007.09 – 2016.12	------	------	------
MetOp-B	2013.08 – 2020.11	------	------	------
MetOp-C	2019.07 – 2020.11	------	------	------
MetOp-A & -B Overlap	2013.08 – 2016.12	-0.0037, 0.3129, 0.9998	0.0251, 0.3443, 0.9998	0.0055, 0.2623, 0.9999
MetOp-B & -C Overlap	2019.07 – 2020.11	-0.0165, 0.4637, 0.9995	0.0092, 0.5068, 0.9995	-0.0043, 0.3878, 0.9997

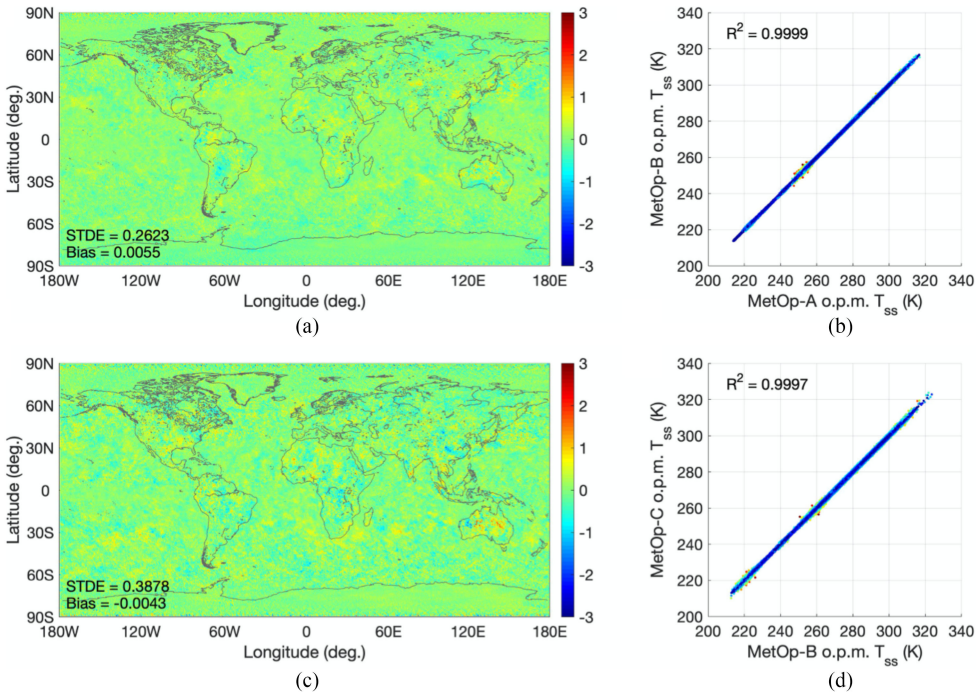

Fig. 2. Bias distribution of o.p.m. T_{ss} (a) between MetOp-A and -B from August 2013 to December 2016, (b) the correlation between MetOp-A and -B o.p.m T_{ss}. Similar to (a) and (b), (c) and (d) are between MetOp-B and -C during their overlapping period from July 2019 to present (November 2020).

as listed in Table I. In order to use the data from all three MetOp satellites for T_{ss} trend monitoring, IASI global monthly mean T_{ss} between MetOp-A and -B (and between MetOp-B and -C) are intercompared and evaluated during their overlapping period. For monthly and spatially gridded mean T_{ss} of MetOp ascending and descending combined measurements, Fig. 2(a) plots the mean bias between MetOp-A and -B overlapping period mean (o.p.m.) T_{ss} in a grid resolution of 0.5°-latitude-longitude, and Fig. 2(b) plots o.p.m. T_{ss} correlation between MetOp-A and -B. Similar plots between MetOp-B and -C are shown in Fig. 2(c) and (d). The STD of bias data plotted in Fig. 2(a) (between MetOp-A and -B) is slightly smaller than that from Fig. 2(c) (between MetOp-B and -C) as the overlapping period of MetOp-A and -B is longer than that of MetOp-B and -C. Data similar to that plotted in Fig. 2, in terms of global mean bias, STDE, and R^2, for ascending and descending nodes are summarized in Table I. These biases, we believe, were mainly introduced by the retrieval error caused by the cloud variation when measurements were taken 50 min apart by two MetOp satellites. However, current IASI Level-1C (L1C) data used here are from different EUMETSAT calibration versions; this inconsistency, further discussed in Section IV, may also contribute to T_{ss} bias. Overall T_{ss} cross-satellite biases are very small and insignificant in global T_{ss} trend analysis; however, they are still applied in T_{ss} trend analysis when three MetOp satellites' data are used. Thus, all three MetOp satellites enable a long-term continuity monitoring global T_{ss} from space.

Monthly mean spatially gridded T_{ss} datasets are assembled. Fig. 3 presents, for example, monthly 0.5°-latitude-longitude gridded T_{ss} of MetOp ascending, descending, and ascending–descending combined measurements for January 2012, respectively. T_{ss} is simultaneously retrieved with ε_ν to guarantee its accuracy [17]. ε_ν associated with Fig. 3(c) for example at a wavenumber of 975 cm^{-1} is plotted in Fig. 3(d) (very similar emissivity from ascending or descending nodes are not plotted). Satellite-derived quantities such as IASI monthly T_{ss} distribution (shown in Fig. 3) have an advantage in terms of global coverage versus ground station, ship, or buoy measurements. Utilizing satellite data limits the error and uncertainty introduced from data interpolation required for using other more spatially

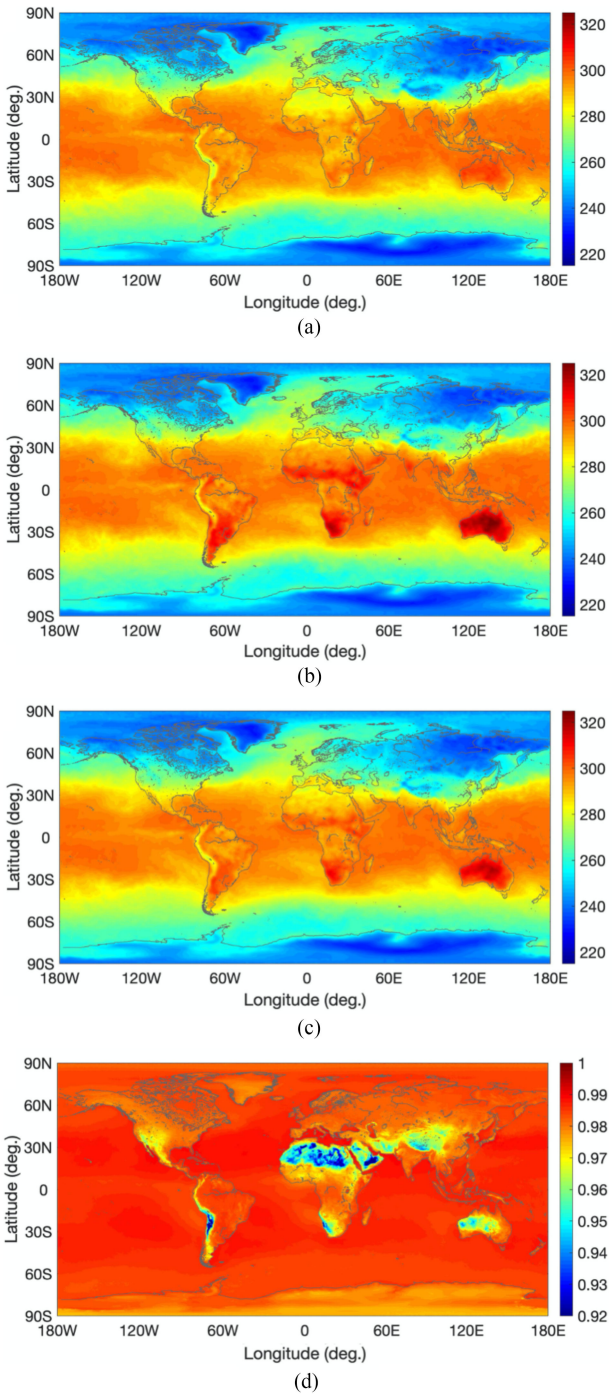

Fig. 3. January 2012 IASI monthly mean T_{ss} (K). (a) MetOp ascending orbits. (b) MetOp descending orbits. (c) MetOp ascending and descending combined. (d) Associated emissivity at 975 cm^{-1} from combined nodes.

sparse data sources, but it also introduces some albeit small uncertainties such as cloud contamination in the data presented in this article. It is noted that retrieved T_{ss} is the average of the effective temperature of the IFOV of a remote sensor, depending on a combination of the surface type and amount of vegetation and underlying bare soil. Also, in the presence of opaque clouds, inferred measurement cannot penetrate the clouds down to the surface; these measurements are detected and not used in this

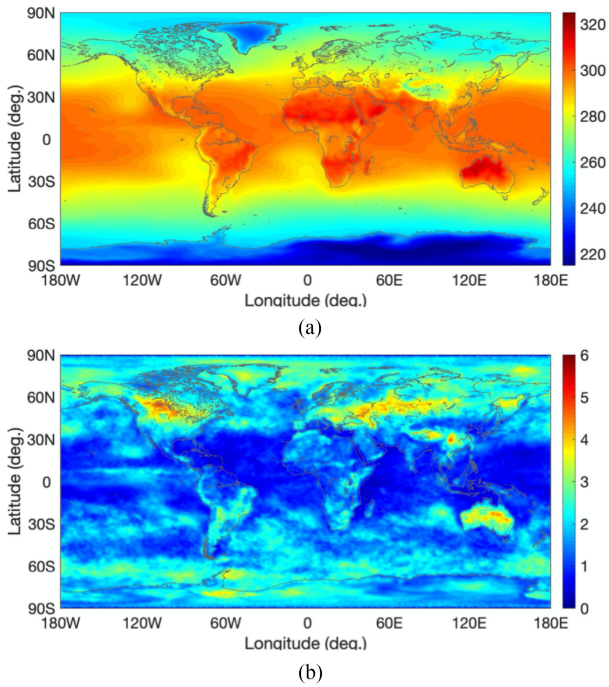

Fig. 4. (a) October T_{ss} climatology (K) from MetOp IASI measurements. (b) Its associated STD from the analysis period.

article. The presence of opaque clouds does affect the accuracy of T_{ss}. Here, we assume that the bias induced by opaque clouds is small and negligible in the monthly gridded-mean data because T_{ss} varies much slower than clouds. It is worth mentioning that this bias does hardly affect T_{ss} anomalies used for its trend estimation since the climatology data, addressed in the following section, is produced in the same manner.

III. Climatology and Anomaly

Global distribution of T_{ss} can be in the range of 190–340 K. In order to monitor a small change of T_{ss} on the order of a few percentages of a degree, it is necessary to look into its anomaly (i.e., seasonal-cycle removed) that is the deviation from its climatological value. We have built up an IASI climatology for T_{ss} based on a current time series of IASI T_{ss}. For instance, IASI ascending (descending or combined node) T_{ss} monthly climatology is the mean of IASI ascending (descending or combined node) T_{ss} of the month from the analysis period. The advantage of using IASI climatology is that the T_{ss} bias error is roughly canceled (or removed) in an anomaly as the same retrieval data are used. Noting that IASI is continuing to take measurements, IASI climatology will be slightly changed as the database expands. IASI T_{ss} climatology for each month has been generated; for example, Fig. 4(a) shows IASI October T_{ss} climatology from MetOp ascending–descending combined measurements from last 14 years, and Fig. 4(b) shows its associated STD from the analysis period. At this point, IASI data from MetOp ascending–descending combined nodes are used for demonstration. Results from ascending or descending data are very similar and will be given in Section IV.

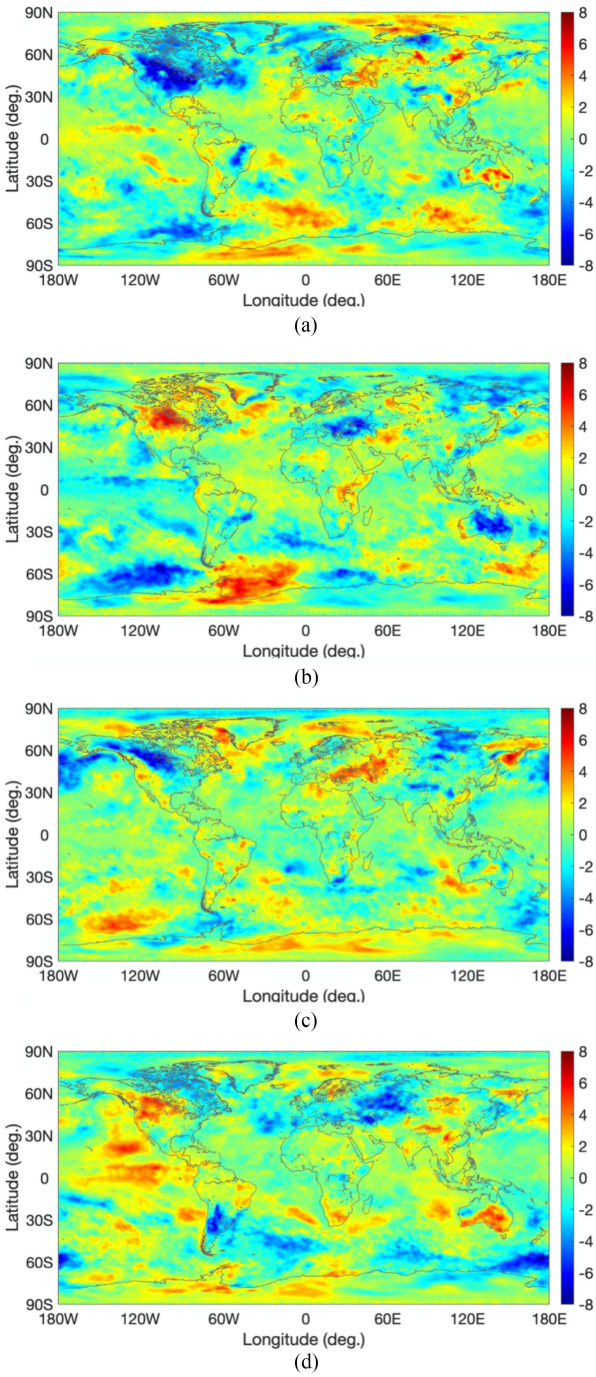

Fig. 5. October monthly mean T_{ss} anomalies (K) from (a) 2009, (b) 2010, (c) 2012, and (d) 2015.

Some October global distribution samples of T_{ss} anomalies relative to a period of IASI climatology [as shown in Fig. 4(a)] are plotted in Fig. 5. T_{ss} retrieved from IASI were investigated to reflect some phenomena such as the well-known El Niño Southern Oscillation (ENSO) [31]. During the typically strong El Niño (2009 and 2015) and La Niña (2010) seasons, the sea surface temperature anomaly patterns in the Pacific equatorial region (plotted in Fig. 5) are very similar to the NOAA optimum interpolation SST (sea surface temperature) analysis [32]. In the equatorial western Pacific Ocean, warmer and cooler T_{ss} were

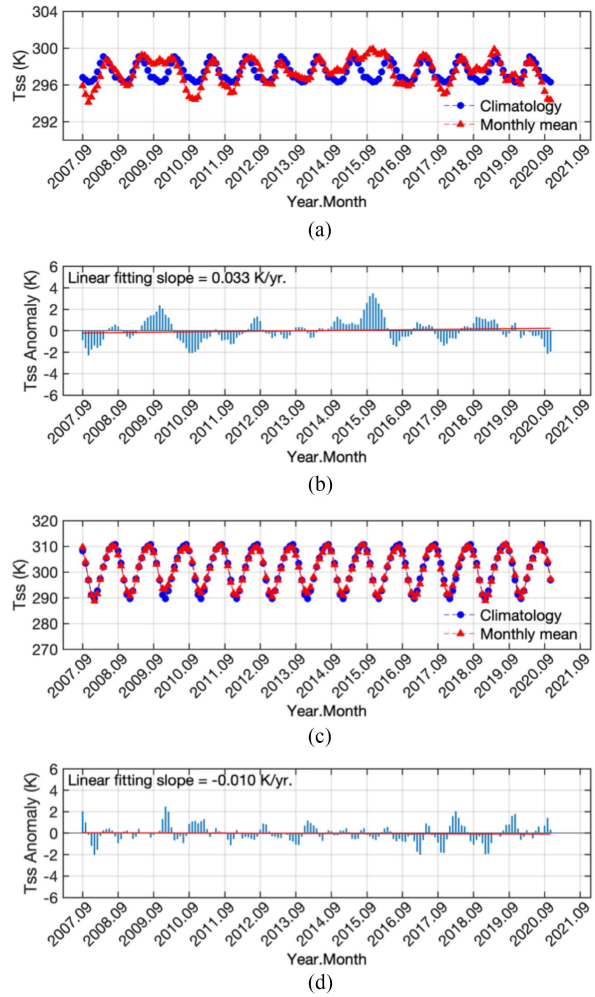

Fig. 6. (a) IASI monthly mean T_{ss} and T_{ss} climatology and (b) T_{ss} anomalies (blue bars) with a linear-least-squares fitting line (in red) at (0 °N, 135 °W). Similar to (a) and (b), (c), and (d) are the plots from a different grid at (20°N, 25°E).

also observed during El Niño (2009 and 2015) and La Niña (2010) seasons, respectively. Correspondingly, Australian land is warmer/dryer during El Niño and cooler/wetter during La Niña [31]. In contrast, Fig. 5(c) plots an example when ENSO activity is minimal. It is noted that some larger T_{ss} anomalies are not from ENSO activities in the Pacific equatorial region. The T_{ss} anomalies are variable within a wild-range from location to location.

From a perspective of temporal variations, two grid-locations were selected just as examples to demonstrate T_{ss} monthly time-series and its trend calculation from the anomalies (i.e., the monthly T_{ss} and associated climatology). Fig. 6(a) plots T_{ss} monthly time-series from a grid point at latitude 0°N and longitude 135°W together with IASI T_{ss} climatology at the same location. Its seasonal-cycle and interannual variations are clearly evident. Again, ENSO activity is revealed from this grid point; for instance, El Niño associated warmer temperatures are indicated during 2009 and 2015, and La Niña associated cooler temperatures during 2010 are also shown. Fig. 6(b) plots T_{ss} anomalies; a linear-least-squares fitting line of T_{ss} anomalies

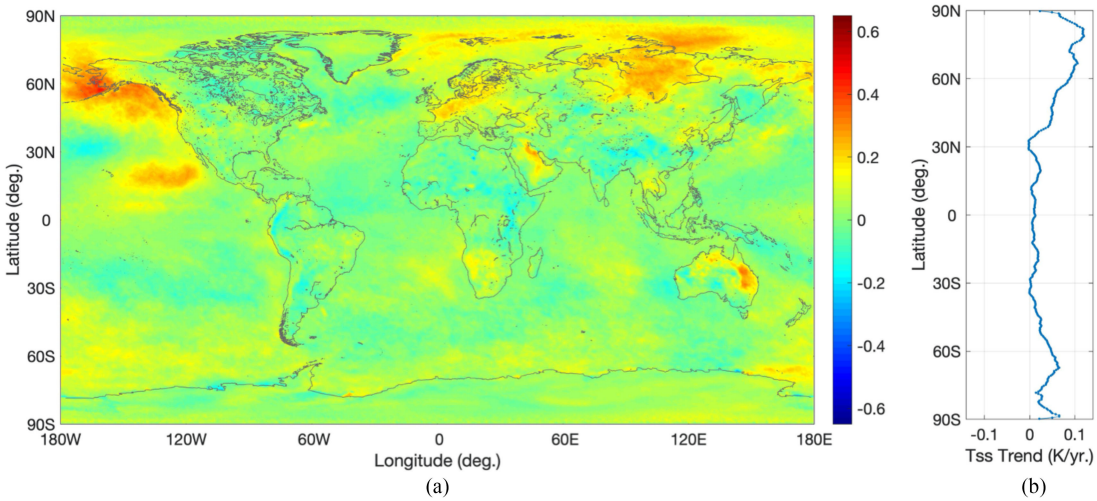

Fig. 7. (a) Distribution of T_{ss} trends (K/yr.) over the analysis period. (b) T_{ss} longitude-mean-trend as a function of latitude.

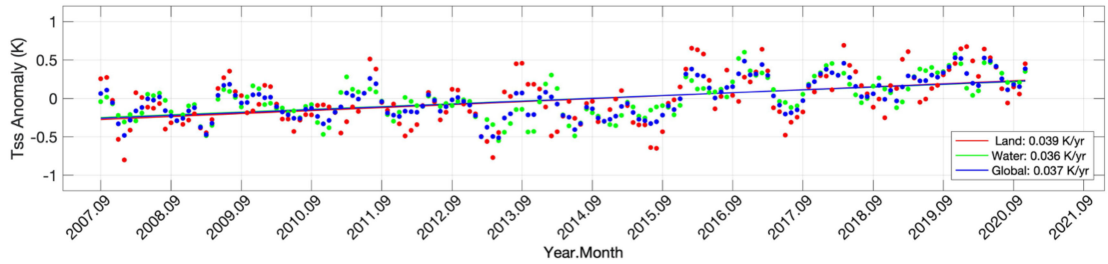

Fig. 8. Month-to-month time-series of T_{ss} anomaly mean over land (red), water (green), and global (blue) coverage; and their linear-least-squares fitting lines.

is plotted in red with a slope of 0.033 K/yr. indicating T_{ss} warming trend at this grid point during that period. This location is chosen to show ENSO natural variability as well as its change during that analysis period. Other locations or regions can be randomly selected for monitoring T_{ss} variations. For instance, a sample from the grid point at latitude 20°N and longitude 25°E is plotted in Figs. 6(c) and (d) and shows a T_{ss} cooling trend of -0.010 K/yr. during our analysis period.

IV. Trend and Discussion

At each grid point, a linear-least-squares fitting slope of T_{ss} anomalies from the analysis period has been computed. A distribution of T_{ss} anomaly trends is plotted in Fig. 7(a). Regional cooling and/or warming from location to location is evidently observed from a maximum cooling rate of -0.208 K/yr. located at 29.25°N latitude, 94.75°E longitude to a maximum warming rate of 0.450 K/yr. located at 57.25°N latitude, 161.25°W longitude. The geophysical distribution of T_{ss} trends [see Fig. 7(a)] is coherent indicating its signal-to-noise level is high enough to be employed for global or regional climate monitoring and trend estimation. For example, T_{ss} trends of southern and northern hemispheres are observable at 0.023 K/yr. and 0.049 K/yr., respectively. T_{ss} trend over the arctic region (latitude $>$ 65°N) is 0.103 K/yr., while T_{ss} trend of 0.011 K/yr. is in the tropical region (20°S $<$ latitude $<$ 20°N). From Fig. 7(a), T_{ss} longitude-mean-trend as a function of latitude is plotted in Fig. 7(b), showing that there has been warming throughout our analysis period in almost all latitudes and significantly pronounced in a higher latitude region. Another way of looking at the T_{ss} trend is to spatially average T_{ss} anomalies, then compute their linear-least-squares fitting slope. This gives a perspective of temporal monthly variability from a single grid point (as shown in Fig. 6) to a regional and/or global scale. As plotted in Fig. 7(a), T_{ss} trend can be obtained in an area of interest. For example, it can be separated from land to water; Fig. 8 plots the T_{ss} trend over land, water, and global mean with a rate of 0.039 K/yr., 0.036 K/yr., and 0.037 K/yr., respectively, from the analysis period.

The uncertainty of the global T_{ss} trend is dependent on the accuracy of gridded-monthly mean T_{ss} anomalies. As indicated in Section III, the bias error is nearly zero (or removed) in an anomaly and the STDE for ascending–descending combined data in a single grid point is estimated to be less than 0.20 K. The STDE for a global averaged T_{ss} anomaly should be much smaller than that of a single grid point. Here, we assume T_{ss} uncertainty from a grid point to a global mean is from 0.30 to 0.10 K including 0.10 K possible unforeseeable uncertainty. Thus, the error of T_{ss} anomaly can be random-number-generated. Based on the error of T_{ss} anomaly and the length of time, an uncertainty for T_{ss} trend from a grid point to a global mean is estimated

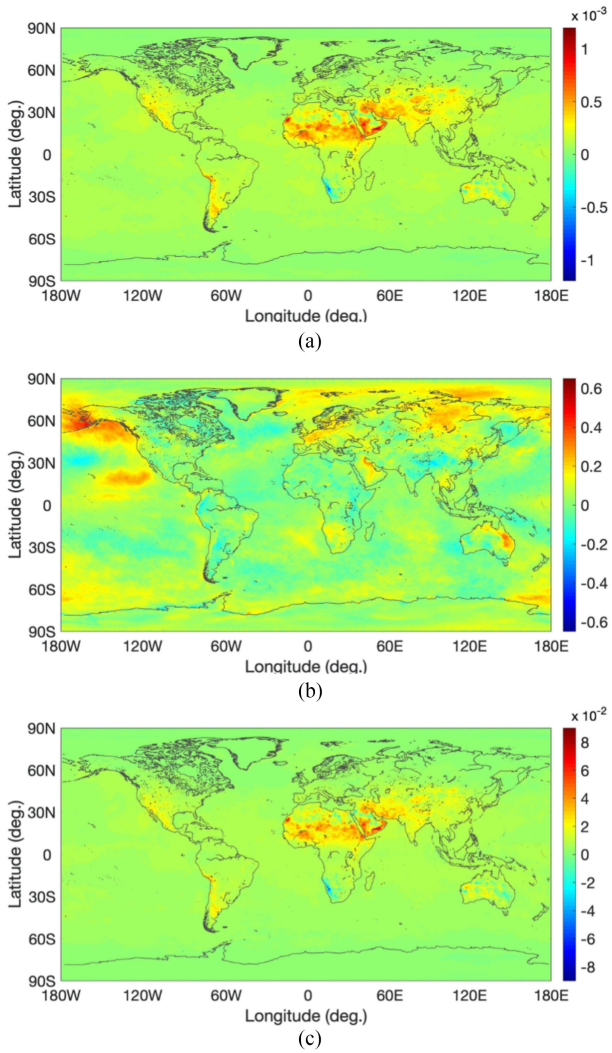

Fig. 9. (a) Global distribution of 975 cm^{-1} ε_ν trends (1/yr.) over the analysis period. (b) Distribution of T_{ss} trends (K/yr.) over the analysis period when associated emissivity trends are assumed to be zeroes. (c) T_{ss} trend differences (K/yr.) associated with emissivity trends when assumed to be zeroes (see text).

to be 0.007 to 0.002 K/yr., respectively. As the length of time period increases, the uncertainty for T_{ss} trend will decrease. The analysis on global T_{ss} retrieved from IASI measurements of MetOp ascending–descending combined node has shown a T_{ss} trend uncertainty of $\pm$0.002 K/yr. over the analysis period.

As surface ε_ν is a key parameter to T_{ss} retrieval accuracy from TIR measurements, ε_ν trend analysis is also performed using emissivity simultaneously retrieved with T_{ss} from the same IASI measurement; an example is shown in Fig. 1. We have chosen ε_ν at 975 cm^{-1} to illustrate its trend distribution as plotted in Fig. 9(a). This ε_ν trend distribution is associated with the T_{ss} trend distribution of Fig. 7(a). A globally averaged ε_ν trend of 8.5×10^{-5}1/yr. is derived, which was mostly contributed by desert regions. A nonzero emissivity trend is realistic. The relationship between emissivity and soil moisture has been studied and shows that a positive (or negative) emissivity trend over land implies a wet (or dry) soil moisture trend [33]. At this point, no independent emissivity dataset is available to validate the emissivity trend; we assume that the emissivity trend derived in this article is physically accurate. The T_{ss} trend currently reported in this communication is derived along with its associated ε_ν trend. Otherwise, T_{ss} trend would be increased (or decreased) to account for a positive (or negative) ε_ν trend. Similar to Fig. 7(a), the global distribution of T_{ss} trends is plotted in Fig. 9(b) when ε_ν trends are assumed to be zeroes. T_{ss} trend differences associated with ε_ν trends for not being zeroes are plotted in Fig. 9(c), which is the difference between Figs. 7(a) and 9(b). For example, in the case presented in Fig. 9, the global mean T_{ss} trend could be increased by 4.9×10^{-3} K/yr. if ε_ν trend was assumed to be zero. As shown in Fig. 9(c), T_{ss} trends would change significantly in some locations over land where the absolute values of emissivity trends are relatively greater.

The uncertainty of T_{ss} trend derived from IASI radiance also relies on the constancy of IASI radiance calibration through this analysis period. IASI L1C processing is conducted by the EUMETSAT. It has been improved over time, but the whole dataset has not yet been reprocessed backward. IASI radiance has been evaluated by Bouillon *et al*. [34] using IASI radiance records from 2007–2017. During that period, improvements were made in an IASI L1C processing software. They concluded that the radiance difference between different calibration versions is 0.02% (or 0.02 K) in the spectral region of 700–1200 cm^{-1}. This spectral region contains surface T_{ss} and ε_ν information. We have estimated that the 0.02% radiance difference, due to calibration improvements, propagates to $\sim 1.3 \times 10^{-4}$ K/yr. T_{ss} trend error which is insignificant in comparison with other error sources.

In Fig. 10, data analyzed by the NASA GISS are used as an independent quasi-reference for comparison to show global monthly T_{sa} anomaly and its trend. GISS T_{sa} anomalies used here are estimated based on meteorological station data with additional ocean temperature data from ships and buoys [2]. T_{sa} anomalies are downloaded from the GISS website [35]. In order to compare them with IASI T_{ss} anomalies, an offset of T_{sa} anomaly mean during the IASI period is applied to the original GISTEMP T_{sa} anomalies (i.e., w.r.t. the analysis period). Fig. 10 plots IASI T_{ss} anomalies and GISTEMP T_{sa} anomalies. The STDE and coefficient of determination (R^2) between two datasets are shown in the figure to give a numerical measure of the comparison. Considering two different physical measures of surface temperature, they still correspond positively to each other to a certain degree (i.e., $R^2 = 42\%$) as they are linked to each other through the complex land-atmosphere processes [36]. Both datasets show global warming with rates of 0.037$\pm$0.002 K/yr. and 0.038 K/yr. from MetOp/IASI T_{ss} and GISTEMP T_{sa} analyses, respectively. Surface skin temperature T_{ss} changes might be different from surface air temperature T_{sa}, explained by the fact that the thermal inertia of Earth's surface is different from that of air. Nevertheless, it is within an expected accuracy and the quantitative comparison of warming rates of T_{ss} and T_{sa} may not be significant as these two terms are physically different especially over land [6], [7].

Similar data analyses from MetOp ascending and descending data also have been performed. As shown in Fig. 11, a global T_{ss} trend with a rate of 0.038$\pm$0.003 K/yr. and 0.035$\pm$0.003 K/yr. is

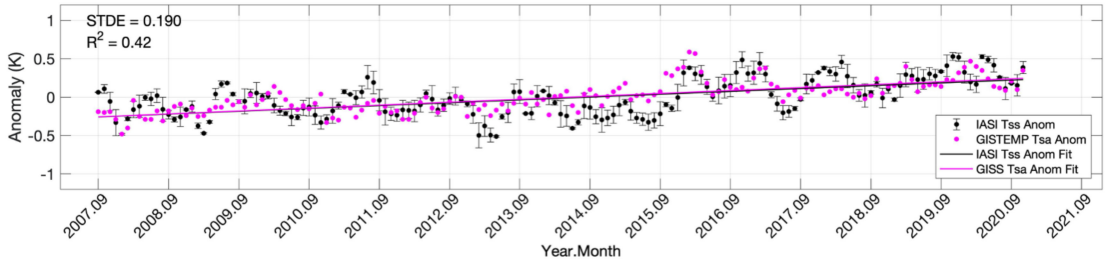

Fig. 10. Monthly global anomalies of IASI T_{ss} and GISTEMP T_{sa} with their linear-least-squares fitting rates of 0.037 K/yr. (in black) and 0.038 K/yr. (in pink), respectively.

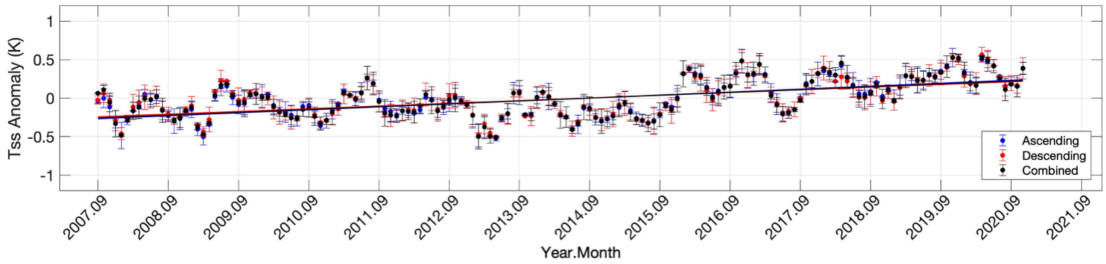

Fig. 11. Global-mean T_{ss} monthly-time-series anomaly trends over the analysis period obtained from MetOp/IASI ascending, descending, and ascending–descending combined measurements, respectively.

TABLE II
IASI T_{SS} TRENDS (K/YR.) OBSERVED OVER GLOBAL AND REGIONAL AREAS

	Ascending Node	Descending Node	Combined Nodes
Global	0.038	0.035	0.037
Water	0.035	0.036	0.036
Land	0.045	0.034	0.039
S. Hemisphere	0.023	0.023	0.023
N. Hemisphere	0.053	0.046	0.049
Arctic region[#]	0.104	0.100	0.103
Tropical region[%]	0.015	0.011	0.011
Antarctic region[+]	0.039	0.035	0.037

[#]Lat.>65°N; [%]20°S<Lat.<20°N; [+]Lat.<65°S

achieved from MetOp ascending and descending measurements, respectively. Table II summarizes MetOp/IASI T_{ss} trends of global and some regional areas from MetOp ascending, descending, and combined node. The trends are very similar between MetOp ascending, descending, and combined nodes; most of them are within estimated uncertainty. A warming trend is significantly pronounced in the northern hemisphere and boosted over the arctic region to a rate of about 0.1 K/yr.

In terms of climatological studies, the time period presented here is limited. Values of trends reported here should be taken with respect to the time period. We noted that the 13+ years of IASI data currently available might not be long enough to perfectly account for all-natural variability (i.e., solar irradiance and sunspot cycles) to claim a climate change [37]. However, it certainly provides a sufficiently long time series from the same satellite measurements to give a clean dataset for monitoring the Earth's environment, assisting climate studies, and supporting the outcomes of global warming trend analyses routinely performed by other research groups such as NASA GISS. IASI on MetOp satellites will continue making the measurements to about the year 2025 or beyond [38]. More than 18 years of IASI measurements from three MetOp satellites in the same orbit would enable assessment and derivation of climate trends for global T_{ss} and other geophysical parameters.

V. CONCLUSION

Satellites have provided a global coverage of time-series measurements. Simultaneous retrieval of Earth's surface skin temperature and emissivity from TIR spectra is critical to achieving highest retrieval accuracy, and a proper cloud detection within a retrieval scheme is essential to filter out the data influenced by cloud attenuation. Several major summary items and conclusions can be obtained from this article.

1) Surface skin temperature and emissivity are simultaneously retrieved from IASI measurements. A current 13+ years of IASI dataset from MetOp satellites has been processed to produce a monthly spatially gridded dataset. Retrieval error is estimated and reduced by the larger sample number in monthly spatial-grids. T_{ss} anomaly for each grid-point and month is computed to derive its trend.
2) Cross-satellite measurements from MetOp series are evaluated enabling the continuity of long-term monitoring.
3) T_{ss} time-series-retrievals are used to calculate the trend. As derived from the IASI T_{ss} analysis, a global distribution of its trends has revealed regional warming and/or cooling in its grid-resolution of 0.5° of latitude-longitude.
4) A globally averaged trend assessment has yielded a warming rate of 0.037±0.002 K/yr. over our analysis period from IASI T_{ss} analysis. This warming trend is more

pronounced in the northern hemisphere as shown in Fig. 7. The global warming rate from this past decade has doubled from what was reported in 2010 starting from 1970s [2].

5) The ε_ν trends simultaneously derived with T_{ss} trends from the same IASI measurements are also presented [e.g., Fig. 9(a)] with a detailed discussion on how ε_ν trends could affect T_{ss} trends when TIR measurements are used.
6) IASI global T_{ss} trend is comparable with NASA GISTEMP global T_{sa} trend. Satellite-derived Earth's surface skin temperature and its warming trend give a unique perspective relative to the surface air temperature trend that is consistent with traditional global surface temperature monitoring analyses of NASA GISS.

This article demonstrates the utility of using Earth's surface skin temperature retrieved from satellite TIR measurements for monitoring regional and/or global surface characteristics. A long-term monitoring of the Earth's surface environment can be critical in assisting weather and climate research. Satellite data shown in this article provide consistent global measurements, which limit the uncertainty of incomplete spatial coverage and/or inconsistent measurements. Satellite measurements can be used as a means of long term and large-scale monitoring of the Earth's environment for climate studies. IASI will continue to provide measurements from MetOp satellites, providing a greater dataset to monitor global climate change. Surface skin temperatures and emissivity are routinely retrieved from IASI measurements to update trend analyses at the NASA Langley Research Center. Similar measurements from other satellite sensors, such as AIRS and CrIS, can also be used to produce T_{ss} analyses as presented in this communication. T_{ss} obtained from multisatellite ultraspectral measurements (i.e., AIRS, IASI series, CrIS series, and future ultraspectral sensors) can extend and ensure consistent inferences for a better climatology database to provide global climatological analyses and environmental monitoring capability. Retrieving, analyzing, and monitoring surface skin temperature trends from such advanced ultraspectral infrared sounders will continue in our future efforts.

ACKNOWLEDGMENT

The authors would like to acknowledge Dr. Mitch Goldberg of NOAA JPSS Program Science Office and Dr. Jack Kaye of NASA's Science Mission Directorate for their continued, enabling support of the NAST-I program. IASI was developed and built under the responsibility of the Centre National d'Etudes Spatiales (CNES). It is flown onboard the MetOp satellites as part of the EUMETSAT Polar System (EPS). The IASI L1C data were received through NOAA Comprehensive Large Array-data Stewardship System (CLASS). The GISS surface temperature was obtained from GISS website.

REFERENCES

[1] L. A. Vincent, X. L. Wang, E. J. Milewska, H. Wan, F. Yang, and V. Swail, "A second generation of homogenized Canadian monthly surface air temperature for climate trend analysis," *J. Geophys. Res.*, vol. 117, no. D18, Sep. 2012, Art. no. D18110.

[2] J. Hansen, R. Ruedy, M. Sato, and K. Lo, "Global surface temperature change," *Rev. Geophys.*, vol. 48, no. 4, Dec. 2010, Art. no. RG4004.

[3] J. L. Høyer and I. Karagali, "Sea surface temperature climate data record for the North Sea and Baltic Sea," *J. Climate*, vol. 29, no. 7, pp. 2529–2541, Mar. 2016.

[4] R. A. Pielke Sr. *et al.*, "Unresolved issues with the assessment of multidecadal global land surface temperature trends," *J. Geophys. Res.*, vol. 112, no. D24, Dec. 2007, Art. no. D24S08.

[5] R. J. H. Dunn, D. M. Stanitski, and N. Gobron, and K. M. Willett, "Global climate," [in 'State of the climate in 2018'] *Bull. Amer. Meteor. Soc.*, vol. 100, no. 9, pp. S5–S68, Sep. 2019.

[6] Z.-L. Li *et al.*, "Satellite-derived land surface temperature: Current status and perspectives," *Remote Sens. Environ.*, vol. 131, pp. 14–37, Apr. 2013.

[7] M. Jin and R. E. Dickinson, "Land surface skin temperature climatology: Benefitting from the strengths of satellite observations," *Enviorn. Res. Lett.*, vol. 5, no. 4, Nov. 2010, Art. no. 041002.

[8] D. K. Zhou *et al.*, "Second SNPP Cal/Val campaign: Environmental data retrieval analysis," *Proc. SPIE*, vol. 9880, May 2016, Art. no. 988008.

[9] M. T. Chahine *et al.*, "AIRS: Improving weather forecasting and providing new insights on greenhouse gases," *Bull. Amer. Meteorol. Soc.*, vol. 87, no. 7, pp. 911–926, Jul. 2006.

[10] K. D. Klaes *et al.*, "An introduction to the EUMETSAT polar system," *Bull. Amer. Meteorol. Soc.*, vol. 88, no. 7, pp. 1085–1096, Jul. 2007.

[11] F. Hilton *et al.*, "Hyperspectral earth observation from IASI: Five years of accomplishments," *Bull. Amer. Meteorol. Soc.*, vol. 93, no. 3, pp. 347–370, Mar. 2012.

[12] M. Divakarla *et al.*, "The CrIMSS EDR algorithm: Characterization, optimization, and validation," *J Geophys. Res.*, vol. 119, no. 8, pp. 4953–4977, Jan. 2014.

[13] Z. M. Wan and Z.-L. Li, "A physics-based algorithm for retrieving land-surface emissivity and temperature from EOS/MODIS data," *IEEE Trans. Geosci. Remote Sens.*, vol. 35, no. 4, pp. 980–996, Jul. 1997.

[14] J. Li, J. Li, E. Weisz, and D. K. Zhou, "Physical retrieval of surface emissivity spectrum from hyperspectral infrared radiances," *Geophys. Res. Lett.*, vol. 34, no. 16, Aug. 2007, Art. no. L16812.

[15] E. Péquignot, A. Chédin, and N. A. Scott, "Infrared continental surface emissivity spectra retrieved from AIRS hyperspectral sensor," *J. Appl. Meteorol. Climatol.*, vol. 47, pp. 1619–1633, Jun. 2008.

[16] D. K. Zhou *et al.*, "All weather IASI single field-of-view retrievals: Case study—Validation with JAIVEx data," *Atmos. Chem. Phys.*, vol. 9, no. 6, pp. 2241–2255, Mar. 2009.

[17] D. K. Zhou *et al.*, "Global land surface emissivity retrieved from satellite ultraspectral IR measurements," *IEEE Trans. Geosci. Remote Sens.*, vol. 49, no. 4, pp. 1277–1290, Apr. 2011.

[18] V. García-Santos, C. Coll, E. Valor, R. Niclòs, and V. Caselles, "Analyzing the anisotropy of thermal infrared emissivity over arid regions using a new MODIS land surface temperature and emissivity product (MOD21)," *Remote Sens. Environ.*, vol. 169, pp. 212–221, Nov. 2015.

[19] D. K. Zhou *et al.*, "Thermodynamic product retrieval methodology for NAST-I and validation," *Appl. Opt.*, vol. 41, no. 33, pp. 6957–6967, Nov. 2002.

[20] D. K. Zhou, A. M. Larar, and X. Liu, "Global surface skin temperature analysis from recent decadal IASI observations," *Proc. SPIE*, vol. 10780, Oct. 2018, Art. no. 1078005.

[21] W. L. Smith Sr. *et al.*, "Technical note: Evolution, current capabilities, and future advances in satellite ultra-spectral IR sounding," *Atmos. Chem. Phys.*, vol. 9, no. 15, pp. 5563–5574, Aug. 2009.

[22] J. P. Taylor *et al.*, "EAQUATE—An international experiment for hyperspectral atmospheric sounding validation," *Bull. Amer. Meteorol. Soc.*, vol. 89, no. 2, pp. 203–218, Feb. 2008.

[23] D. K. Zhou *et al.*, "Retrieval validation during the European aqua thermodynamic experiment," *Quart. J. Roy. Meteorol. Soc.*, vol. 133, no. S3, pp. 203–215, Dec. 2007.

[24] W. L. Smith, Sr., *et al.*, "The NPOESS airborne sounding testbed interferometer—Remotely sensed surface and atmospheric conditions during CLAMS," *J. Atmos. Sci.*, vol. 62, pp. 1118–1134, Apr. 2005.

[25] L. L. Strow, S. E. Hannon, S. De Souza-Machado, H. E. Motteler, and D. Tobin, "An overview of the AIRS radiative transfer model," *IEEE Trans. Geosci. Remote Sens.*, vol. 41, no. 2, pp. 303–313, Feb. 2003.

[26] D. C. Tobin *et al.*, "Atmospheric radiation measurement site atmospheric state best estimates for atmospheric infrared sounder temperature and water vapor retrieval validation," *J. Geophys. Res.*, vol. 111, no. D9, Mar. 2006, Art. no. D09S14.

[27] N. Pougatchev *et al.*, "IASI temperature and water vapor retrievals—Error assessment and validation," *Atmos. Chem. Phys.*, vol. 9, no. 17, pp. 6453–6458, Aug. 2009.

[28] A. M. Larar *et al.*, "IASI spectral radiance validation inter-comparisons: Case study assessment from the JAIVEx field campaign," *Atmos. Chem. Phys.*, vol. 10, no. 2, pp. 441–430, Jan. 2010.
[29] D. K. Zhou, A. M. Larar, X. Liu, W. L. Smith Sr., and L. L. Strow, "Error consistency analysis scheme for ultraspectral sounding retrieval error budget estimation," *Remote Sens. Lett.*, vol. 4, no. 3, pp. 219–227, Aug. 2012.
[30] S. A. Safieddine *et al.*, "Artificial neural networks to retrieve land and sea skin temperature from IASI," *Remote Sens.*, vol. 12, no. 17, Aug. 2020, Art. no. 2777.
[31] D. K. Zhou, A. M. Larar, and X. Liu, "MetOp-A/IASI observed continental thermal IR emissivity variations," *IEEE J. Sel. Topics Appl. Earth Observ. Remote Sens.*, vol. 6, no. 3, pp. 1156–1162, Jun. 2013.
[32] Optimum Interpolation Sea Surface Temperature (OISST). Accessed: Jul. 15, 2020. [Online]. Available: https://www.ncdc.noaa.gov/oisst
[33] D. K. Zhou, A. M. Larar, and X. Liu, "On the relationship between land surface infrared emissivity and soil moisture," *J. Appl. Remote Sens.*, vol. 12, no. 1, Mar. 2018, Art. no. 016030.
[34] M. Bouillon *et al.*, "Ten-year assessment of IASI radiance and temperature," *Remote Sens.*, vol. 12, no. 15, Jul. 2020, Art. no. 2393.
[35] NASA GISS Surface Temperature Analysis, GISTEMP, version 4. Accessed: Dec. 14, 2020. [Online]. Available: https://data.giss.nasa.gov/gistemp
[36] T. Suni *et al.*, "The significance of land-atmosphere interactions in the Earth system–iLEAPS achievements and perspectives," *Anthropocene*, vol. 12, pp. 69–84, Dec. 2015.
[37] B. A. Wielicki *et al.*, "Achieving climate change absolute accuracy in orbit," *Bull. Amer. Meteorol. Soc.*, vol. 94, no. 10, pp. 1519–1539, Oct. 2013.
[38] K. D. Klaes, F. Montagner, and C. Larigauderie, "Metop-B, the second satellite of the EUMETSAT polar system, in orbit," in *Proc. SPIE*, vol. 8866, Sep. 2013, Art. no. 886613.

Daniel K. Zhou received the Ph.D. degree in physics from Utah State University, Logan, UT, USA, in 1992.

He is a Physical Scientist with the Chemistry and Dynamics Branch, Science Directorate, NASA Langley Research Center, Hampton, VA, USA. He has more than 30 years of experience with hyperspectral interferometer remote sensing measurements and data processing. He has worked on numerous programs such as the Cryogenic Infrared Radiance Instrumentation for Shuttle (CIRRIS-1A), National Airborne Sounder Testbed Interferometer (NAST-I), and the Infrared Atmospheric Sounding Interferometer (IASI), and is currently involved in several remote sensing programs. His experience includes retrieval algorithm development for meteorological and trace gas profile retrieval from remotely sensed infrared measurements, as well as retrieval analyses and validation. His recent research includes deriving global land surface emissivity spectra, temperatures, and soil moisture from satellite infrared measurements in support of Earth observations and climate studies.

Dr. Zhou has received numerous awards including the NASA Exceptional Achievement Medal.

Allen M. Larar received the Ph.D. degree in atmospheric and space sciences from the University of Michigan, Ann Arbor, in 1993.

He is currently an Associate Director for Research and Mission Science with Science Directorate, NASA Langley Research Center, Hampton, VA, USA. He has over 25 years of experience of advancing passive remote sensing measurement capabilities. His research interests concentrate on remote sensing of thermodynamic state and trace species composition, and he has had extensive involvement in most aspects regarding the development and implementation of advanced passive remote sensing technology for Earth atmosphere measurement applications. He was the Principal Investigator of the Tropospheric Trace Species Sensing-Fabry–Perot Interferometer Instrument Incubator Program, successfully completed in 2006, that developed an imaging Fabry–Perot interferometer system, mitigating risks for future geostationary-based measurement of tropospheric ozone. He is currently involved in several remote sensing programs, developing or employing advanced Michelson and Fabry–Perot interferometer systems on ground-, aircraft-, and space-based platforms.

Xu Liu received the Ph.D. degree in physical chemistry from the University of Denver, Denver, CO, USA, in 1989.

He is currently a Physical Scientist with the Chemistry and Dynamics Branch, Science Directorate, NASA Langley Research Center, Hampton, VA, USA. He has developed algorithms for radiometric calibration, instrument line shape characterization, fast radiative transfer models, and atmospheric parameter retrievals for various instruments ranging from microwave to visible spectral range. He has served as a member on various government teams and performed collaborated work with international partners on remote sensing. He has developed a superfast principal-component-based radiative transfer model, which has been successfully applied to hyperspectral sensors such as national airborne sounder testbed interferometer, infrared atmospheric sounding interferometer, atmospheric infrared sounder, cross-track infrared sounder, and the climate absolute radiance and refractivity observatory.

Dr. Liu has received numerous awards such as National Science Foundation Antarctic Service Award, NASA Superior Accomplishment Award, NASA Performance Award, NASA Inventions and Contributions Board Awards, and NASA Exceptional Achievement Medal.